remote sensing

MDPI

Article

Gridless DOA Estimation with Extended Array Aperture in Automotive Radar Applications

Pengyu Jiang [1,2,3], Silin Gao [1,2,3], Jie Zhao [4], Zhe Zhang [1,2,5,6,7,*] and Bingchen Zhang [1,2,3]

[1] Key Laboratory of Technology in Geo-Spatial Information Processing and Application System, Chinese Academy of Sciences, Beijing 100190, China
[2] Aerospace Information Research Institute, Chinese Academy of Sciences, Beijing 100094, China
[3] School of Electronic, Electrical and Communication Engineering, University of Chinese Academy of Sciences, Beijing 100049, China
[4] Beijing Autoroad Tech Company, Ltd., Beijing 100012, China
[5] Suzhou Key Laboratory of Microwave Imaging, Processing and Application Technology, Suzhou 215000, China
[6] Suzhou Aerospace Information Research Institute, Suzhou 215000, China
[7] National Key Laboratory of Microwave Imaging Technology, Beijing 100190, China
* Correspondence: zhangzhe01@aircas.ac.cn

Abstract: Millimeter-wave automotive radar has become an essential tool for autonomous driving, providing reliable sensing capabilities under various environmental conditions. To reduce hardware size and cost, sparse arrays are widely employed in automotive radar systems. Additionally, because the targets detected by automotive radar typically exhibit sparsity, compressed sensing-based algorithms have been utilized for sparse array reconstruction, achieving superior performance. However, traditional compressed sensing algorithms generally assume that targets are located on a finite set of grid points and perform sparse reconstruction based on predefined grids. When targets are off-grid, significant off-grid errors can occur. To address this issue, we propose an automotive radar sparse reconstruction algorithm based on accelerated Atomic Norm Minimization (ANM). By using the Iterative Vandermonde Decomposition and Shrinkage Threshold (IVDST) algorithm, we can achieve fast ANM, which effectively mitigates off-grid errors while reducing reconstruction complexity. Furthermore, we adopt a Generalized Likelihood Ratio Test (GLRT) detector to eliminate noise and clutter in the automotive radar operating environment. Simulation results show that our proposed algorithm significantly improves reconstruction accuracy compared to the iterative soft threshold (IST) algorithm while maintaining the same computational complexity. The effectiveness of the proposed algorithm in practical applications is further validated through real-world data experiments, demonstrating its superior capability in clutter elimination.

Keywords: millimeter-wave automotive radar; sparse linear array; difference co-array; atomic norm minimization (ANM); GLRT detector

check for updates

Academic Editor: Pedro Melo-Pinto

Received: 30 October 2024
Revised: 21 December 2024
Accepted: 23 December 2024
Published: 26 December 2024

Citation: Jiang, P.; Gao, S.; Zhao, J.; Zhang, Z.; Zhang, B. Gridless DOA Estimation with Extended Array Aperture in Automotive Radar Applications. *Remote Sens.* **2025**, *17*, 33. https://doi.org/10.3390/rs17010033

Copyright: © 2024 by the authors. Licensee MDPI, Basel, Switzerland. This article is an open access article distributed under the terms and conditions of the Creative Commons Attribution (CC BY) license (https://creativecommons.org/licenses/by/4.0/).

1. Introduction

Millimeter-wave automotive radars have become a crucial component of advanced driver assistance systems (ADAS) in recent decades [1–3]. Millimeter-wave radar, unlike systems dependent on environmental light or weather conditions, ensures consistent road safety for all participants, day and night [4–6]. At the same time, compared to ground-based and airborne radar, automotive radar imposes stricter requirements on cost, size, and data processing speed. Therefore, the progression of automotive radar technology

cannot rely solely on increasing antenna aperture length or the number of antennas, as these approaches are constrained by practical limitations [7–9]. Adopting sparse strategies for optimizing array configurations and using suitable reconstruction algorithms to process sparse array signals have become critical in automotive radar development [10–12].

Common sparse linear array (SLA) includes minimum redundancy array [13], co-prime array [14], and nested array [15]. These arrays offer advantages such as ease of implementation and well-designed structures. In recent years, sparse linear array antenna has been applied to automotive radar to reduce the cost and computational complexity. For instance, Yang et al. [7] proposed a sparse planar array optimization method based on a genetic algorithm for automotive radar. Sun and Zhang [11] applied sparse array to a two-dimensional array, achieving four-dimensional sensing for autonomous driving. Correas-Serrano and González-Huici [8] used several different sparse array configurations to evaluate the direction of arrival (DoA) estimation performance of different algorithms in automotive radar. Compared to uniform linear array (ULA) with full array elements, the missing elements in SLA typically result in reduced radar performance. To mitigate this limitation, researchers have introduced the concept of difference co-array. By constructing a virtual difference co-array using sparse array elements, it is possible to effectively expand the number of array elements, mitigating the negative effects of missing elements in SLA [15,16].

In terms of reconstruction algorithms, compressed sensing (CS) has gained considerable popularity in automotive radar due to its exceptional capability for reconstructing under-sampled signals [8,11,17–20]. By using compressed sensing algorithms to process signals obtained from SLA, the problem of high sidelobes can be effectively addressed while achieving super-resolution capability. Traditional compressed sensing algorithms use a discretized reconstruction model and assume that the scatterer precisely falls on a predefined grid. However, in practical applications, this assumption does not always hold true and discretized reconstruction models inevitably introduce off-grid errors [21]. One approach to solve this issue involves increasing grid density [22–24]. However, this approach substantially increases computational complexity, leading to prohibitively long sparse reconstruction times.

To address the off-grid effect, researchers introduced the concept of atomic norm [25] and used atomic norm minimization (ANM) to identify unknown frequencies from under-sampled data. ANM represents the signal as a linear combination of continuous atoms and achieves sparse reconstruction by minimizing the atomic norm. Hence, ANM has the advantages of both gridless reconstruction and super-resolution, enabling accurate reconstruction of signals obtained from SLA [26–29]. The computation of ANM is typically formulated into a semidefinite programming (SDP) problem, which is usually solved by the CVX toolbox. However, the CVX toolbox utilizes interior-point methods to search for the optimal solution along feasible paths, which is notably slow [30]. The significant computational overhead restricts the potential application of the ANM algorithm in the field of automotive radar.

The preceding analysis indicates that employing sparse linear array in automotive radar effectively reduces the number of antennas, thereby decreasing costs and physical dimensions. However, the missing array elements in this approach also lead to reconstruction performance degradation. Furthermore, while the ANM algorithm can be utilized for sparse reconstruction to mitigate off-grid effects, it significantly increases computational time. To address these challenges associated with SLA in automotive radar systems, we propose a novel sparse array automotive radar imaging method based on accelerated ANM.

Firstly, for SLA automotive radar systems, we obtain the virtual array of the sparse array through difference co-array. By extracting information from the difference array

elements, we derive a virtual array with an extended aperture and an increased element count, effectively enhancing the capabilities of sparse array. Subsequently, we introduce the Iterative Vandermonde Decomposition and Shrinkage Threshold (IVDST) algorithm [31,32]. This innovation eliminates the need for SDP solutions, reducing computational complexity from $\mathcal{O}(N^{3.5})$ to $\mathcal{O}(N^2)$, where N represents the number of array elements. Consequently, it meets the real-time processing requirements of automotive radar systems. Finally, we also recognize that the working environment of automotive radar is not only filled with Gaussian white noise but also with various types of clutter interference. These interferences include clutter generated by weak targets that are not of interest within the radar's line of sight, as well as clutter caused by multipath propagation [33]. Given the unknown and constantly changing interference in the scene, we use a Generalized Likelihood Ratio Test (GLRT) detector to adaptively detect and suppress interference in the reconstructed results [34–37]. This method effectively suppresses noise and clutter interference, further improving reconstruction performance. The algorithm proposed in this article achieves high-resolution reconstruction results through fast processing, while effectively reducing the impact of environmental noise and clutter. The main contributions of this paper are summarized as follows:

- We apply the difference co-array to automotive radar, reducing the number of elements while maintaining imaging performance.
- We introduce the IVDST algorithm into automotive radar imaging for the first time, which not only addresses the off-grid problem but also significantly enhances processing speed, meeting the high real-time requirements of automotive radar.
- We introduce the GLRT detector for the first time. In complex automotive radar operating environments, this detector can effectively suppress clutter and improve imaging quality.

This paper is organized as follows. Section 2 provides an overview of the automotive radar signal model. Taking nested arrays as an example, we demonstrate the construction of difference co-array for SLA and introduce the concept of differential element information. Section 3 introduces the ANM reconstruction algorithm based on SDP and then proposes an ANM reconstruction algorithm based on IVDST. Additionally, we describe the application of the GLRT detector for further processing of the reconstruction results. Section 4 presents simulation experiments that validate the effectiveness of our proposed method. Section 5 presents the reconstruction results of two sets of real-world data. Finally, Section 6 summarizes our research and future work.

2. Signal Model

We consider a uniform linear array with uniform spacing d. Some elements in this array are missing, and the actual number of elements is N, thus forming a sparse array, as shown in Figure 1. Assuming the incident signal originates from the far field, it can be approximated as a plane wave upon arrival at the array, with an incident angle of θ_k. Assuming there are K incident signal sources originating from K distinct directions. The incidence angle set can be written as $\{\theta_k\}_{k=1}^{K}$, and the received signal vector $\mathbf{x}$ can be expressed as [38]:

$$\mathbf{x} = \sum_{k=1}^{K} c_k \mathbf{a}(\theta_k) + \mathbf{n} \tag{1}$$

where $\mathbf{a}(\theta_k)$ is the array manifold of this linear array, c_k is the complex amplitude of the k-th signal, $\mathbf{n}$ is the Gaussian noise and clutter. The array manifold $\mathbf{a}(\theta_k)$ can be expressed as:

$$\mathbf{a}(\theta_k) = \left[1 \quad \exp(j2\pi \tfrac{D_1 \sin\theta_k}{\lambda}) \quad \cdots \quad \exp(j2\pi \tfrac{D_N \sin\theta_k}{\lambda})\right]^{\mathrm{T}} \tag{2}$$

where $D = [D_1, D_2, \cdots, D_N]$ is the position of sparse array elements, λ is the wavelength of the signal and $(\cdot)^T$ is the transpose operator.

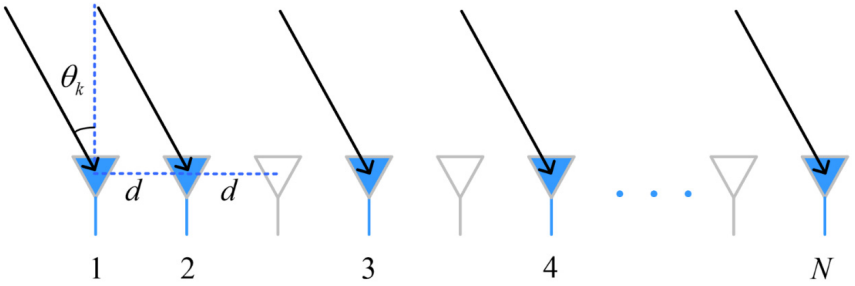


Figure 1. Schematic diagram of sparse array automotive radar.

We employ the two-level nested array [11] as the sparse array configuration. When compared with other sparse arrays, nested arrays present several notable advantages. Their configuration design is simple and easy to implement [15]. Additionally, the difference co-array generated by nested array exhibits uniformity and continuity, which is exceptionally conducive to subsequent reconstruction processes [39]. A nested array is composed of two sub-arrays arranged in front and back, namely dense subarray and sparse subarray, as shown in Figure 2. The number of dense array elements is N_1 and the distance between elements is d. The number of sparse array elements is N_2 and the distance between elements is $(N_1 + 1)d$. The total number of array elements is $N = N_1 + N_2$. The explicit expressions of nested array are as follows [15]:

$$\mathbb{S} = \{id, 1 \leq i \leq N_1\} \cup \{j(N_1 + 1)d, 1 \leq j \leq N_2\}. \tag{3}$$

The aperture length of nested array with $N_1 + N_2$ elements is expanded to $2N_2(N_1 + 1) - 1$.

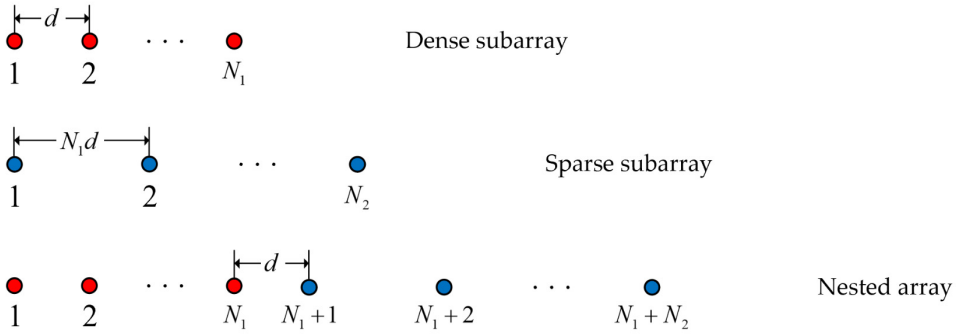


Figure 2. Schematic diagram of nested array. ●: array element of dense subarray ●: array element of sparse subarray.

The difference co-array of nested array can be represented as the set of all possible differences between the positions of the physical array elements:

$$\Omega = \{D_{m1} - D_{m2}, 1 \leq m1, m2 \leq N\} \tag{4}$$

where D_{m1} and D_{m2} are the position of any array elements. A uniform virtual array with a more extended aperture can be obtained through the difference co-array. As shown in Figure 3, a nested array with $N_1 = 4, N_2 = 2$ can achieve 19 virtual array elements.

In conclusion, the utilization of nested array can effectively optimize ULA and reduce the number of physical array elements. Concurrently, by leveraging difference co-array, we can establish a superior-performance virtual array that mitigates the negative impacts on reconstruction performance caused by the decreased count of physical array elements.

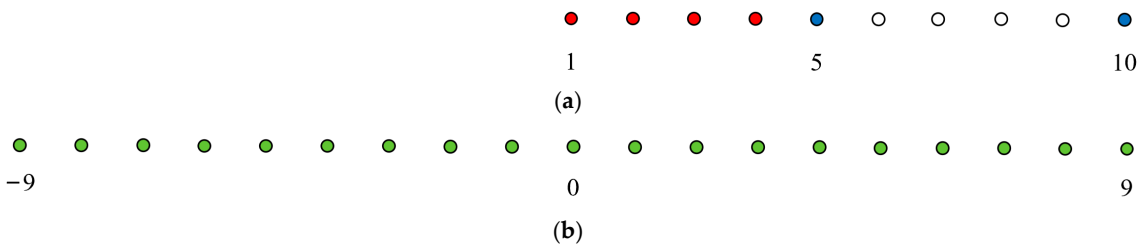


Figure 3. Examples of difference co-array for nested array: (**a**) nested array; (**b**) difference co-array. ●: array element of dense subarray ●: array element of sparse subarray ○: vacant array element ●: difference co-array element.

Considering that the number of potential target resolution cells significantly exceeds the actual number of targets in an automotive environment, we can reconstruct the received signal through compressed sensing. Traditionally, the observation scenario is divided into L grid points, with the set of angles represented by the grid points as $\theta = [0, 2\pi/L, \cdots, 2\pi(L-1)/L]$, where $L \gg K$. The one-dimensional reconstruction model of the received signal is [38]:

$$\mathbf{x} = \sum_{l=1}^{L} c_l \mathbf{a}(\theta_l) + \mathbf{n} = \mathbf{A}(\theta)\mathbf{c} + \mathbf{n} \tag{5}$$

where $\mathbf{A}(\theta) = [\mathbf{a}(\theta_1), \mathbf{a}(\theta_2), \cdots, \mathbf{a}(\theta_L)]$ is the measurement matrix of the reconstruction model and $\mathbf{c} = [c_1, c_2, \cdots, c_L]^{\mathrm{T}}$ is the observation scenario. Furthermore, to fully utilize the advantages of nested array with long virtual apertures, we need to extract information from the virtual array elements.

Assuming the received signals from different directions are uncorrelated, the covariance matrix of $\mathbf{x}$ is given by:

$$\mathbf{X} = \mathrm{E}(\mathbf{x}\mathbf{x}^{\mathbf{H}}) = \mathbf{A}\mathrm{diag}(\mathbf{p})\mathbf{A}^{\mathbf{H}} + \mathbf{n}^2\mathrm{I} \tag{6}$$

where $\mathrm{diag}(\mathbf{p})$ is a diagonal matrix, whose main diagonal element $\mathbf{p} = \left[|p_1|^2, \ldots, |p_L|^2\right]^{\mathrm{T}}$ is the power distribution of the observation scenario. I is the identity matrix and $(\cdot)^{\mathbf{H}}$ is the Hermitian transpose operator. In practice, the covariance matrix is commonly obtained by averaging the data received from multiple observations. The element in row i and column j of the covariance matrix $\mathbf{X}$ can be expressed as:

$$X_{i,j} = \mathrm{E}\left(x_i x_j^{\mathrm{H}}\right) = \sum_{l=1}^{L} p_l^2 \exp\left(-j2\pi\left(D_i - D_j\right)\sin\theta_l/\lambda\right) \tag{7}$$

where $D_i - D_j$ is the distance from the i-th element to j-th element. Thus, virtual array elements can be constructed based on the position differences of array elements, and the information of virtual array elements can be extracted using the covariance matrix. Then, we vectorize the covariance matrix $\mathbf{X}$:

$$\mathbf{z} = vec(\mathbf{X}) = \mathbf{B}\mathbf{p} + \mathbf{n}_{vec} \tag{8}$$

where $vec(\cdot)$ means vectorizing the matrix, $\mathbf{B}$ is the measurement matrix with $\mathbf{B} = \mathbf{A}^* \odot \mathbf{A} = \left[\mathbf{a}(\theta_1)^* \otimes \mathbf{a}(\theta_1), \mathbf{a}(\theta_2)^* \otimes \mathbf{a}(\theta_2), \cdots, \mathbf{a}(\theta_L)^* \otimes \mathbf{a}(\theta_L)\right]$, $\odot$ denotes the Khatri–Rao product, $\otimes$ denotes the Kronecker product and $(\cdot)^*$ denotes the conjugate operator. In matrix $\mathbf{X}$, some elements correspond to identical positional differences due to the array's symmetric structure. It is necessary to eliminate the duplicate elements within $\mathbf{z}$ and rearrange the remaining elements to obtain $\bar{\mathbf{z}}$. Taking nested array as an example, its difference co-array

is composed of virtual array elements from $-N_2(N_1+1)$ to $N_2(N_1+1)$. After removing the elements at the repeated positions from $\mathbf{z}$, we can obtain $\overline{\mathbf{z}}$:

$$\overline{\mathbf{z}} = \left[\mathbf{z}_{-(N_1+1)N_2}, \mathbf{z}_{-(N_1+1)N_2+1}, \cdots, \mathbf{z}_{-1}, \mathbf{z}_0, \mathbf{z}_1, \cdots, \mathbf{z}_{(N_1+1)N_2-1}, \mathbf{z}_{(N_1+1)N_2}\right]. \tag{9}$$

$\overline{\mathbf{z}}$ can be considered as a received signal of a virtual linear array (VLA). Hence, we can perform sparse reconstruction of $\mathbf{p}$ by solving the optimization problem:

$$\hat{\mathbf{p}} = \underset{\mathbf{p}}{\operatorname{argmin}} \frac{1}{2}\left\|\overline{\mathbf{z}} - \overline{\mathbf{B}}\mathbf{p}\right\|_2^2 + \|\mathbf{p}\|_\alpha \tag{10}$$

where $\overline{\mathbf{B}}$ represents the measurement matrix after row elimination and row rearrangement, and α is the regularization term. It should be noted that the current model does not yet account for multipath propagation. In applications where suppression of multipath propagation is required, it can be integrated with algorithms such as spatial smoothing [40].

3. Reconstruction Algorithm

3.1. ANM Method

In traditional grid-based sparse reconstruction algorithms, direction of arrival (DOA) estimation is performed using Equation (10). However, in practice, the incident angles often do not lie on these grid points, which leads to reconstruction errors. As a result, we introduce the atomic norm to enhance the reconstruction accuracy.

As a gridless CS approach, ANM enables the reconstruction of off-grid targets from compressive measurements [41]. Building upon Equation (8), it can be expressed as:

$$\mathbf{z} = \sum_{k=1}^{K} p_k\left(\mathbf{a}(\theta_k)^* \otimes \mathbf{a}(\theta_k)\right) + \mathbf{n}_{vec} = \sum_{k=1}^{K} p_k \mathbf{b}(\theta_k) + \mathbf{n}_{vec} \tag{11}$$

where p_k is the power distribution of target k. By performing duplicate element elimination and rearrangement, we can obtain:

$$\overline{\mathbf{z}} = \Theta(\mathbf{z}) = \sum_{k=1}^{K} p_k \overline{\mathbf{b}}(\theta_k) + \overline{\mathbf{n}} \tag{12}$$

where $\Theta(\cdot)$ represents the process of element elimination and rearrangement.

Assuming that the signal $\overline{\mathbf{z}}$ consists of several components. These components have the same support set which belongs to a known atomic norm $\mathcal{B}$ that may have infinite size [42]. By utilizing the atomic set $\mathcal{B} = \left\{\overline{\mathbf{b}}(\theta) : \theta \in (0, \pi)\right\}$, we can define the atomic norm of $\overline{\mathbf{z}}$:

$$\|\overline{\mathbf{z}}\|_{\mathcal{B}} = \inf\left\{\sum_{k=1}^{K} |\hat{p}_k| : \overline{\mathbf{z}} = \sum_{k=1}^{K} \hat{p}_k \overline{\mathbf{b}}(\hat{\theta}_k), \overline{\mathbf{b}}(\hat{\theta}_k) \in \mathcal{B}\right\}. \tag{13}$$

The atomic norm $\|\overline{\mathbf{z}}\|_{\mathcal{B}}$ can be computed via SDP as follows [30]:

$$\begin{aligned} \|\overline{\mathbf{z}}\|_{\mathcal{B}} = \min_{\mathbf{u}, v} &\left\{\tfrac{1}{2}(v + \operatorname{trace}(\mathbf{T}(\mathbf{u})))\right\} \\ s.t. \quad &\begin{pmatrix} v & \overline{\mathbf{z}}^{\mathbf{H}} \\ \overline{\mathbf{z}} & \mathbf{T}(\mathbf{u}) \end{pmatrix} \geq \mathbf{0} \end{aligned} \tag{14}$$

where v is the variables to be optimized and v is a real number, $\mathbf{T}(\mathbf{u})$ is a Toeplitz matrix determined and $\mathbf{u}$ being its first row. In conclusion, we can achieve the gridless reconstruction through ANM, which is given in Algorithm 1.

Algorithm 1: Reconstruction Algorithm via ANM.

Input: $\mathbf{x}$, K

1: Calculate the covariance matrix $\mathbf{X} = \mathrm{E}(\mathbf{x}\mathbf{x}^{\mathbf{H}})$;
2: Vectorize the covariance matrix $\mathbf{X}$ and obtain vector $\mathbf{z}$;
3: Eliminate the duplicate elements within $\mathbf{z}$ and obtain vector $\bar{\mathbf{z}}$;
4: Solve the SDP problem in Equation (14) and obtain matrix $\mathbf{T}(\mathbf{u})$;
5: Apply the root-music algorithm to $\mathbf{T}(\mathbf{u})$ and obtain K roots $\{r_k\}$;
6: Calculate incident angle $\hat{\theta}_k = \arcsin(\lambda r_k/(2\pi d))$;
7: Solve amplitude p_k by least squares method.

Output: $\hat{\theta}_k, p_k$

3.2. ANM Method Based on Accelerated Proximal Gradient

Solving the ANM optimization problem using the SDP method can effectively eliminate the negative impact of off-grid issues on reconstruction performance. However, automotive radar is a radar system with high real-time processing requirements. For a signal of size N, SDP solving brings a computational complexity of $\mathcal{O}(N^{3.5})$. To reduce the computational load while ensuring estimation accuracy, we introduce the IVDST algorithm based on the Accelerated Proximal Gradient (APG) technique [31,43].

First, for a VLA that does not have full array elements, we compute the signal $\mathbf{y}$ obtained from a linear array with all elements (the full array):

$$\mathbf{y} = \mathbf{P}^{\mathrm{H}}\bar{\mathbf{z}} + \mathbf{n} \tag{15}$$

where $\mathbf{P}$ represents the sampling matrix of the VLA relative to the full array. Subsequently, the optimization problem of $\mathbf{y}$ is formulated as follows:

$$\hat{\mathbf{y}} = \underset{\mathbf{y}}{\operatorname{argmin}} \frac{1}{2}\|\mathbf{P}\mathbf{y} - \bar{\mathbf{z}}\|_2^2 + \|\mathbf{y}\|_{\mathcal{B}}. \tag{16}$$

The IVDST algorithm applies iterative shrinkage thresholding to enforce low-rank and positive semi-definite (PSD) properties on the Vandermonde Toeplitz structured matrix $\mathbf{T}(\mathbf{u})$. The idea is to avoid SDP solving thereby reducing computational complexity to $\mathcal{O}(N^2)$.We reformulate the optimization problem as an equivalent unconstrained optimization problem [31]:

$$\min_{\boldsymbol{\alpha}} \boldsymbol{F}(\boldsymbol{\alpha}) = \underbrace{\frac{\mu}{2}\|\mathbf{P}\mathbf{y} - \bar{\mathbf{z}}\|_2^2}_{f(\boldsymbol{\alpha})} + \underbrace{\mathrm{tr}(\mathbf{Z}(\boldsymbol{\alpha})) + \mathcal{C}(\mathbf{Z}(\boldsymbol{\alpha}))}_{g(\boldsymbol{\alpha})} \tag{17}$$

where the variable vector $\boldsymbol{\alpha} = (\mathbf{y}, v, \mathbf{T})$ encompasses all the unknown parameters. The scalar μ serves as a weighting factor that represents the noise threshold ϵ. We define the matrix $\mathbf{Z}(\boldsymbol{\alpha})$ as $\left[v\ \mathbf{y}^{\mathrm{H}}; \mathbf{y}\ \mathbf{T}\right]$, ensuring that its trace satisfies $\mathrm{tr}(\mathbf{Z}(\boldsymbol{\alpha})) = \nu + \mathrm{tr}(\mathbf{T})$. Cost function $\mathcal{C}(\cdot)$ is applied to impose a positive semidefinite structure on $\mathbf{Z}(\boldsymbol{\alpha})$.Within the objective function $\boldsymbol{F}(\boldsymbol{\alpha})$, the term $\boldsymbol{f}(\boldsymbol{\alpha})$ is smooth and differentiable, whereas the atomic norm minimization component $\boldsymbol{g}(\boldsymbol{\alpha})$ is non-smooth. Therefore, we use the APG technique shown in Algorithm 2 to solve the optimization problem.

Algorithm 2: Reconstruction Algorithm via IVDST-ANM for VLA.

Input: $\bar{\mathbf{z}}$, K, $\mathbf{P}$, ϵ

Initialization:

- Initial signal: $\mathbf{y}_0 = \mathbf{P}^{\mathrm{H}}\bar{\mathbf{z}} + \mathbf{n}$
- Sample covariance matrix: $\mathbf{R}_0 = \mathbf{y}_0{\mathbf{y}_0}^{\mathrm{H}}$
- Toeplitz matrix: $\mathbf{T}_0 = \mathrm{Toeplitz}(\mathbf{R}_0)$
- Optimization variables: $\boldsymbol{\alpha_1} = \boldsymbol{\alpha_0} = (\mathbf{y}_0, v_0, \mathbf{T}_0)$
- Momentum parameter: $\mathrm{t}_0 = 1$

Repeat

1: Smoothing: Calculate $\boldsymbol{\alpha}_{\mathrm{bar}} = \boldsymbol{\alpha}_{\mathrm{i}} + \frac{\mathrm{t}_{\mathrm{i}-1}-1}{\mathrm{t}_{\mathrm{i}}}(\boldsymbol{\alpha}_{\mathrm{i}} - \boldsymbol{\alpha}_{\mathrm{i}-1}) = (\mathbf{y}_{bar}, v_{bar}, \mathbf{T}_{bar})$, where $\mathrm{t}_{\mathrm{i}+1} = \frac{1+\sqrt{1+4\mathrm{t}_{\mathrm{i}}^2}}{2}$;

2: Gradient descent: Calculate $\mathbf{y}_g = \mathbf{y}_{\mathrm{bar}} - \delta\mathbf{P}^H(\mathbf{P}\mathbf{y}_{\mathrm{bar}} - \bar{\mathbf{z}})$ and $\mathbf{T}_g = \mathbf{T}_{bar}$, where δ is an appropriate small step;

3: Proximal mapping:

Decompose $\mathbf{T}_g = \mathbf{V}\boldsymbol{\Lambda}\mathbf{V}^H$ and shrink $\boldsymbol{\Lambda}$ to $\widetilde{\boldsymbol{\Lambda}}$, set $\widetilde{\mathbf{T}} = \mathbf{V}\widetilde{\boldsymbol{\Lambda}}\mathbf{V}^H$;

Set $\mathbf{Z} = \left[\mathrm{trace}(\widetilde{\Lambda})\mathbf{y}_g^H; \mathbf{y}_g\mathbf{T}_g\right]$ and decompose $(\boldsymbol{\Sigma}, \mathbf{U}) = \mathrm{eigs}(\mathbf{Z}, \mathrm{rank}(\widetilde{\boldsymbol{\Lambda}}) + 1)$;

Set $\tilde{\mathbf{Z}} = \mathbf{U}\boldsymbol{\Sigma}\mathbf{U}^H$ and update $\boldsymbol{\alpha}_{\mathrm{i}+1} = (\mathbf{y}_{\mathrm{i}+1}, \nu_{\mathrm{i}+1}, \mathbf{T}_{\mathrm{i}+1})$.

Until $i >$ maxiter or $\|\mathbf{T}_{i+1} - \mathbf{T}_i\|_F \leq \epsilon$

Output: $\mathbf{T}$

3.3. GLRT Detector

To perform target detection in automotive radar scenarios with noise and clutter, we introduce the GLRT detector to further process the reconstruction results obtained from the IVDST algorithm, eliminating false reconstructed targets. For the echo signal $\bar{\mathbf{z}}$ received by VLA in Equation (12), the detection problem is formulated as a binary hypothesis test:

$$\begin{cases} H_0 : \bar{\mathbf{z}} = \mathbf{n} \\ H_1 : \bar{\mathbf{z}} = \beta\mathbf{m} + \mathbf{n} \end{cases} \tag{18}$$

where H_0 and H_1 represent the absence or presence of the target, respectively. β is an unknown complex amplitude factor, $\mathbf{m}$ is the array manifold vector of VLA and $\mathbf{n}$ represents the set of all noise, which may include Gaussian white noise, clutter, and others. In practical scenarios, the covariance matrix $\mathbf{R}_n$ of clutter and noise is unknown. Therefore, we select data cells surrounding the cell under test as auxiliary data to estimate the covariance matrix $\mathbf{R_n}$:

$$\mathbf{R_n} = \sum_{l=1}^{L} \mathbf{x}(l)\mathbf{x}^{\mathrm{H}}(l) \tag{19}$$

where L represents the number of selected auxiliary data cells. If the probability density functions under the binary hypotheses are known, the GLRT detector can be expressed as:

$$\frac{\max\limits_{\beta} f_1(\bar{\mathbf{z}}|\beta, \mathbf{R_n})}{f_0(\bar{\mathbf{z}}|\mathbf{R_n})} \underset{H_0}{\overset{H_1}{\gtrless}} \xi \tag{20}$$

where ξ is the detection threshold of the GLRT detector. Then, the joint probability density function of the observations under H_0 is:

$$f_0(\bar{\mathbf{z}}|\mathbf{R_n}) = \frac{1}{(2\pi)^N \det(\mathbf{R_n})} \exp\left(-\frac{1}{2}\bar{\mathbf{z}}^{\mathbf{H}}\mathbf{R_n}^{-1}\bar{\mathbf{z}}\right) \tag{21}$$

where $\det(\cdot)$ denotes the matrix determinant. Similarly, the joint probability density function of the observations under H_1 is:

$$f_1(\bar{\mathbf{z}}|\beta, \mathbf{R_n}) = \frac{1}{(2\pi)^N \det(\mathbf{R_n})} \exp\left(-\frac{1}{2}(\bar{\mathbf{z}} - \beta\mathbf{m})^{\mathbf{H}}\mathbf{R_n}^{-1}(\bar{\mathbf{z}} - \beta\mathbf{m})\right). \tag{22}$$

The GLRT-based detector first uses the maximum likelihood estimation method to estimate the unknown parameter β:

$$\hat{\beta} = \frac{\mathbf{a}^{\mathrm{H}}\mathbf{R_n}^{-1}\bar{\mathbf{z}}}{\mathbf{a}^{\mathrm{H}}\mathbf{R_n}^{-1}\mathbf{a}}. \tag{23}$$

Then, we substitute this estimate into the likelihood ratio detector to calculate the detection statistic [35]:

$$\frac{\left|\mathbf{m}^H\mathbf{R_n}^{-1}\bar{\mathbf{z}}\right|^2}{\mathbf{m}^H\mathbf{R_n}^{-1}\mathbf{m}} \underset{H_0}{\overset{H_1}{\gtrless}} \xi. \tag{24}$$

The introduction of a GLRT detector can help automotive radar eliminate the influence of clutter in complex environments and obtain more accurate reconstruction results.

Figure 4 illustrates the complete flowchart of our proposed algorithm, which is divided into two parts: pre-processing and sparse reconstruction. The pre-processing step extracts virtual array element information from the echo signals, which is followed by sparse reconstruction using the accelerated ANM algorithm. Finally, the GLRT detector is applied to obtain the final reconstruction results.

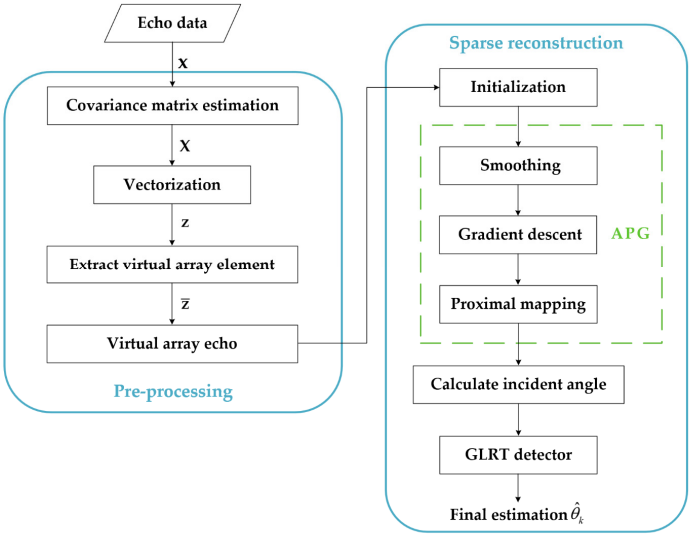


Figure 4. Flowchart of the proposed method.

4. Simulation Experiment Results

In this section, we validate the efficacy of our proposed algorithm through simulation experiments. To demonstrate its superiority, we designed seven sets of comparative experiments focusing on reconstruction performance, noise resistance, convergence speed, stability and super-resolution capability, point target resolution capability, snapshots effect and reconstruction time.

4.1. Reconstruction Performance

We selected four distinct scenarios for comparative analysis. These include the iterative soft threshold (IST) algorithm reconstructing the signal from SLA, the IST algorithm reconstructing the signal from VLA, and our proposed algorithm reconstructing the signal

from SLA and VLA. Here, IST represents the traditional grid-based compressed sensing algorithm, SLA represents direct reconstruction using the sparse array, VLA represents reconstruction from the virtual array and IVDST+VLA represents our proposed method. Additionally, the digital beamforming (DBF) algorithm was included in some experiments as a control. The parameters of the simulation experiment are shown in Table 1.

Table 1. Parameters of the simulation experiments.

Parameters	Value
Frequency	77 GHz
Minimum array element spacing	2 mm
Signal-to-noise ratio	20 dB
Arrangement of array elements	$\{1, 2, 3, 4, 8\}d$
Dense array elements	$\{1, 2, 3\}d$
Sparse array elements	$\{4, 8\}d$

First, the off-grid performance of the DBF algorithm, the IST algorithm, and the IVDST algorithm were evaluated. We adopted an array configuration of $\{1, 2, 3, 4, 8\}d$, set the grid spacing to 5°, and positioned point targets at grid points, as well as 0.5° and 2.5° off-grid. The reconstruction results are shown in Figure 5. When the target is located precisely at grid points, all three algorithms achieve satisfactory reconstruction results. However, for off-grid targets, the IST algorithm exhibits significant energy leakage to adjacent grid points, resulting in considerable reconstruction errors. Moreover, as the target's off-grid displacement increases, the reconstruction error of the IST algorithm also increases. In contrast, the DBF and IVDST algorithms are not affected by grid discretization and can effectively reconstruct off-grid targets. The number of snapshots was set to 100.

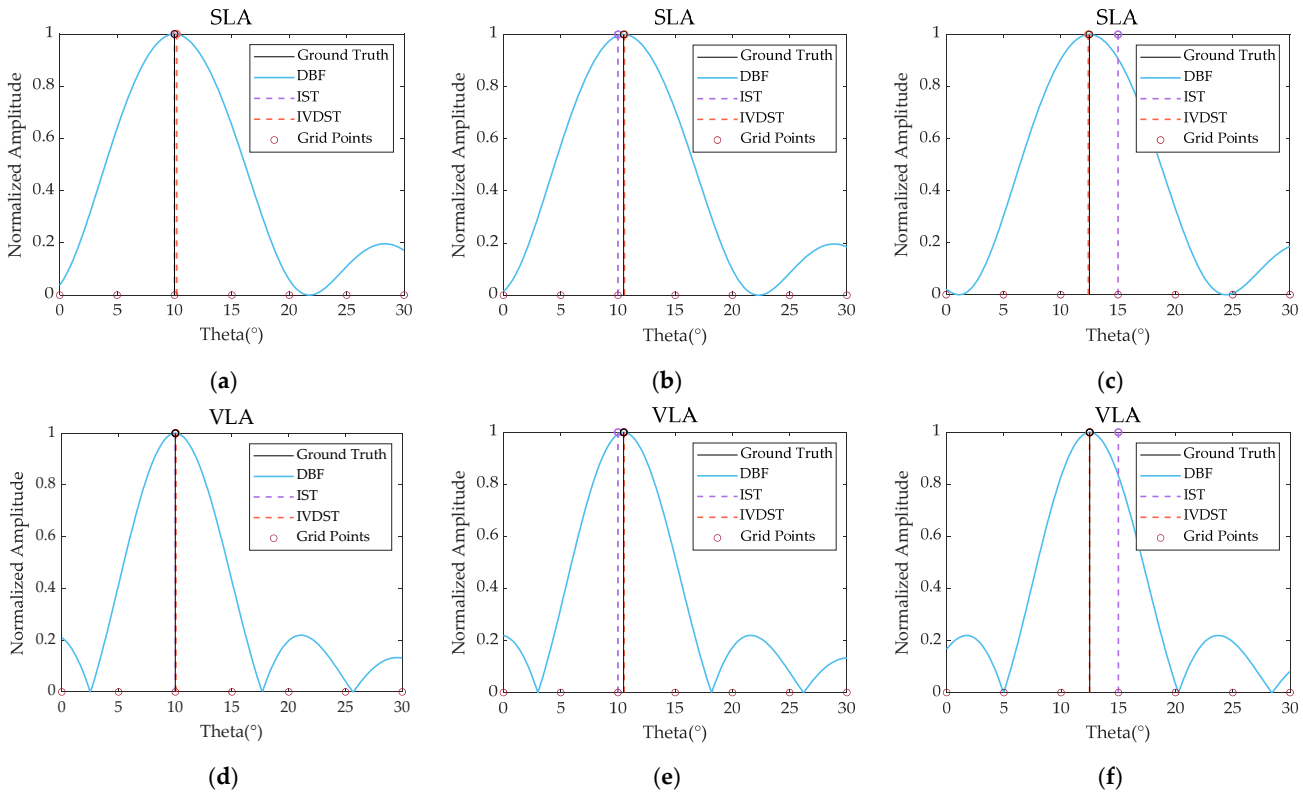


Figure 5. Comparative reconstruction results for DBF, IST and IVDST under varying off-grid conditions. (**a**) SLA with 0° off-grid; (**b**) SLA with 0.5° off-grid; (**c**) SLA with 2.5° off-grid; (**d**) VLA with 0° off-grid; (**e**) VLA with 0.5° off-grid; (**f**) VLA with 2.5° off-grid.

4.2. Noise Resistance

Furthermore, for the IVDST algorithm, the reconstruction results using SLA are inferior to those using VLA. Hence, we conducted detailed comparative experiments on the reconstruction performance of IST and IVDST algorithms through Monte Carlo simulations under two conditions, on-grid and 0.5° off-grid. We introduced relative bias (RB) as an evaluation metric to quantitatively analyze the reconstruction accuracy:

$$RB = \sum_{q}^{Q} \left|\hat{\theta}_q - \theta_q\right| / \left|\theta_q\right| \tag{25}$$

where Q represents the number of Monte Carlo experiments, $\hat{\theta}_q$ represents the estimated value of the target angle in the q-th experiment, and θ_q represents the true value of the target. As shown in Figure 6, the reconstruction performance using VLA is significantly better than SLA for both algorithms. Moreover, the VLA-based algorithm exhibits better noise resistance, and its reconstruction performance is basically not affected by noise. Under on-grid conditions, the reconstruction performance of the IST and IVDST algorithms are comparable. However, in off-grid scenarios, the performance of the IST algorithm is limited by errors induced by grid points, whereas the IVDST algorithm exhibits superior performance.

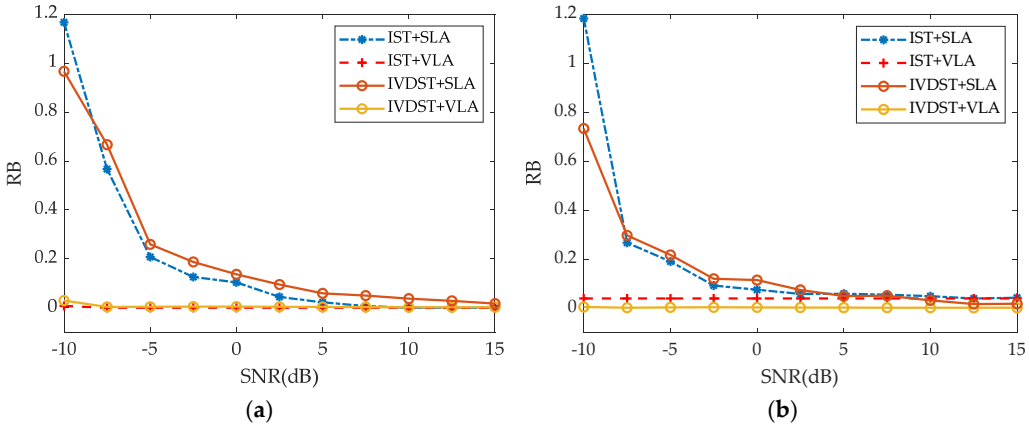


Figure 6. Reconstruction performance curve of IST+SLA, IST+VLA, IVDST+SLA and IVDST+VLA versus the SNR: (**a**) on-grid; (**b**) 0.5° off-grid.

4.3. Convergence Speed

The algorithm proposed in this paper iteratively derives the final reconstruction result. Therefore, the number of iterations is important for evaluating the robustness of our proposed algorithm. In this section, we conducted comparative experiments on the convergence speed under different SNRs, utilizing four different algorithms and a single target point while keeping other parameters constant. The maximum number of iterations was set to 100. Through Monte Carlo simulations, the curve of the number of iterations versus the SNR ratio is shown in Figure 7.

It can be observed that the number of iterations decreases with increasing SNR, with the IST algorithm exhibiting a slightly faster convergence speed compared to the IVDST algorithm. As the SNR increases, the iteration numbers of the four algorithms tend to stabilize. In the case of an SNR of −10 dB, both SLA-based algorithms reached the maximum number of iterations without successfully reconstructing the target. This experiment validates that the algorithm proposed in this invention possesses excellent noise resistance, achieving rapid convergence across different SNR levels.

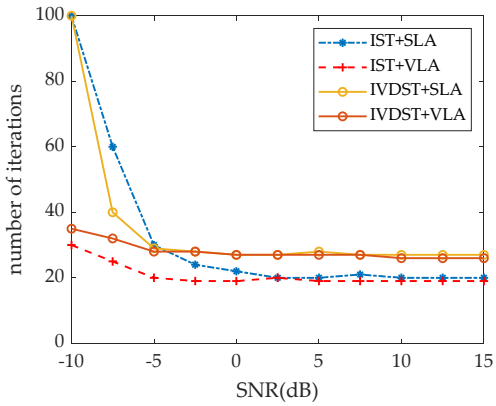


Figure 7. Impact of SNR on convergence speed.

4.4. Stability and Super-Resolution Capability

The advantages of our proposed algorithm were demonstrated. Next, as shown in Table 2, we designed three additional sparse arrays and validated the stability and super-resolution capabilities of our algorithm through experimental scenarios involving two point targets. The Rayleigh angular resolution corresponding to the physical array aperture length is used as the angular resolution for DBF. For IVDST+VLA, two point targets are randomly placed within an angular range of -30° to 30°. The spacing between the two point targets is progressively decreased, and the angle estimates are deemed to achieve effective resolution when the following condition is satisfied:

$$\text{RMSE} = \sqrt{\frac{1}{2}\sum_{i=1}^{2}\left(\hat{\theta}_i - \theta_i\right)^2} < \frac{|\Delta\theta|}{5} \tag{26}$$

where RMSE means root mean square error, $\hat{\theta}_i$ is the estimated value of the point target, θ_i is the true value of the point target, $\Delta\theta$ is the difference from the true value of two point targets. For each spacing value, conduct 100 Monte Carlo simulations. SNR was set to 10 dB. If more than 95% of the cases are successfully resolved, the effective angular resolution of IVDST+VLA is determined.

Table 2. Array parameters and angular resolution of IVDST+VLA.

	Position	**Aperture Length (mm)**	**Missing Virtual Element**	**Angular Resolution of DBF**	**Angular Resolution of IVDST+VLA**	**Super-Resolution Capability**
Array 1	$\{1,2,3,4,8\}d$	$7d$	None	16.0°	11.2°	1.43
Array 2	$\{1,2,3,6,9\}d$	$8d$	None	13.9°	10.1°	1.37
Array 3	$\{1,2,3,6\}d$	$5d$	None	22.4°	16.9°	1.33
Array 4	$\{1,3,5,8\}d$	$7d$	$\pm 1d, \pm 6d$	16.0°	27.6°	0.58

As shown in Table 2, the IVDST+VLA algorithm demonstrates good stability and super-resolution capability. Compared to Array 1, the aperture length of Array 2 has increased, although the number of physical elements remains unchanged. As a result, the physical array becomes more sparse, leading to a slight reduction in its super-resolution capability. For Array 3, the significant reduction in aperture length limits its super-resolution capability. The three arrays all feature continuous virtual arrays, thereby exhibiting robust super-resolution performance. In contrast, Array 4 achieves an aperture length of 7d with only four physical elements, leading to the absence of four virtual elements and consequently lacking super-resolution capability. We conclude that the IVDST+VLA algorithm achieves

super-resolution while reducing the number of array elements. Meanwhile, the design of sparse array is critical, and longer aperture lengths and continuous virtual arrays need to be considered.

4.5. Snapshot Effect

Since information from virtual array elements is extracted through the covariance matrix, the estimation of the covariance matrix is crucial to our proposed algorithm. We selected Array 1, Array 2, and Array 3, which possess super-resolution capabilities in Table 3, to evaluate the impact of the number of snapshots on reconstruction accuracy. A single point target was randomly selected within the range of $-30°$ to $30°$, and the number of snapshots was set to 1, 5, 10, 15, 20, 25, 30, 35, 40, 45, and 50, while other parameters remained consistent with those in the previous simulation experiments. The reconstruction accuracy obtained from 100 Monte Carlo simulations is presented in Figure 8.

Table 3. The positions of each array in MIMO array and equivalent array.

	Position (mm)
MIMO array	$Tx : \{0, 5.7, 11.4\}$ $Rx : \{0, 3.8, 7.6, 11.4\}$
Equivalent array	$\{0, 3.7, 5.7, 7.6, 9.5, 11.4, 13.3, 15.3, 17.1, 19.1, 22.9\}$

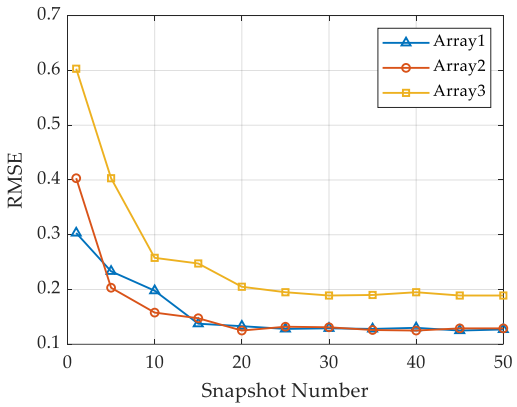


Figure 8. RMSE curves of different snapshot numbers.

It can be observed that as the number of snapshots increases, the reconstruction accuracy of all three arrays improves significantly and tends to stabilize within the range of 20–30 snapshots. Due to the reduction in aperture length and the decrease in the number of virtual array elements, the estimation of the covariance matrix is adversely affected. As a result, the reconstruction accuracy of Array 3 is lower than that of Array 1 and Array 2. In summary, for our proposed algorithm, selecting an appropriate number of snapshots to enhance the estimation of the covariance matrix can effectively improve reconstruction accuracy.

4.6. Point Target Number

Further, we conducted simulation experiments to investigate the impact of the number of targets on the algorithm's performance. The experiments were carried out using Array 1, Array 2, and Array 3 as presented in Table 2. SNR was set to 10 dB, and the number of snapshots was fixed at 100. Within an observation range of $-60°$ to $60°$, the number of point targets gradually increased until the RMSE no longer satisfied the condition specified in Equation (26). To ensure the validity of the results, we controlled the angular separation between point targets to exceed the angular resolution presented in Table 2.

As observed in Figure 9, all three sparse arrays achieved point target resolution capabilities that exceed the number of physical array elements. Arrays 1 and 2 can effectively estimate the DOA of point targets in up to nine different directions using five physical elements. Array 3 can effectively estimate the DOA of up to six point targets in different directions using four physical elements. Within the effective DOA estimation interval, the RMSE exhibited a gradually increasing trend as the number of targets increased. Therefore, the algorithm proposed in this paper can satisfy multi-target DOA estimation for automotive radar in complex scenarios with fewer physical array elements.

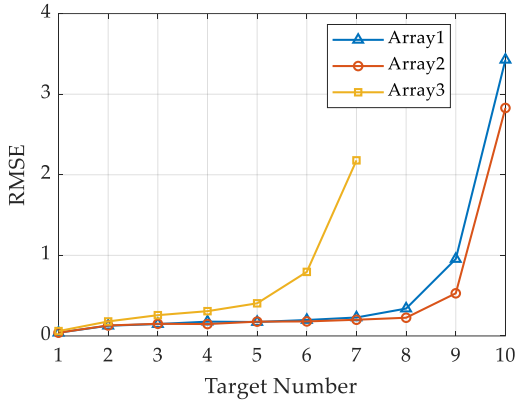


Figure 9. RMSE curves of different target numbers.

4.7. Reconstruction Time

Finally, to validate the acceleration capability of the IVDST algorithm, we fixed the array element spacing at 2 mm and started with an initial array of 10 elements, gradually increasing the number of elements to 100. We compared the computation time of the traditional ANM algorithm (based on SDP) with those of the IVDST algorithm, introducing the IST and the orthogonal matching pursuit (OMP) as representative compressed sensing algorithms and multiple signal classification (MUSIC) as spectral estimation algorithm for comparison.

The experimental result is shown in Figure 10a. As the number of array elements increases, the computation time for the traditional ANM algorithm grows significantly, whereas the computation times for the other four algorithms increase slowly. The increase for IVDST is negligible compared to the traditional ANM algorithm. As shown in Figure 10b, the computational complexity of IVDST remains comparable to that of three other commonly employed DOA estimation algorithms. The computational complexity of IST, music, and IVDST-ANM increases with the number of array elements. In this experiment, which involves only a single point target, the OMP algorithm demonstrates the fastest convergence speed. Consequently, we can conclude that the IVDST algorithm achieves gridless estimation while maintaining the same computational complexity as mainstream DOA estimation algorithms.

Through seven sets of simulation experiments, we derive the following conclusions: Benefiting from a longer virtual aperture and more virtual array elements, the VLA-based algorithm achieves superior reconstruction performance compared to SLA. Additionally, the ANM method effectively addresses the performance degradation issue of grid-based CS algorithms in off-grid scenarios. Furthermore, to address the slow convergence of SDP-based methods, we introduced the IVDST algorithm to solve the atomic norm optimization problem, significantly reducing processing time. In summary, our proposed algorithm achieves substantial improvements in both reconstruction accuracy and processing time.

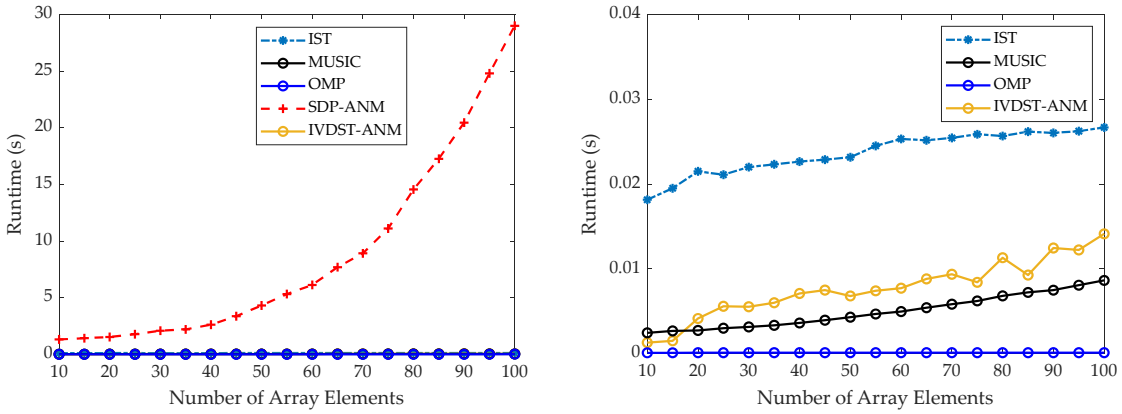


Figure 10. Comparison of processing time under different number of array elements: (**a**) IST, MUSIC, OMP, SDP-ANM and IVDST-ANM; (**b**) IST, MUSIC, OMP, and IVDST-ANM.

5. Real Data Experiment Results

In this section, we validate the practicality of our proposed algorithm for automotive radar systems using real-world data. The experimental data were provided by Autoroad Tech. Co. Ltd., located in Chaoyang District, Beijing, China. We used two different models of radar, referred to as Automotive Radar 1 and Automotive Radar 2. It is noteworthy that the automotive radar we used is not based on nested array or any form of sparse array design. Additionally, we observed that most existing automotive radar antenna array configurations do not typically use common sparse array forms. This is due to various physical constraints on antenna arrangement or because array scarification was not considered during the initial design [44]. Therefore, we selected a subset of array elements to form a sparse array that closely approximates a nested array, resulting in an incomplete nested array. This demonstrates the broad applicability of our proposed algorithm across different array configurations.

First, we employed two corner reflectors to verify the reconstruction performance of our proposed algorithm. Similar to the simulation experiments, we conducted four sets of experiments: IST+SLA, IST+VLA, IVDST+SLA, and IVDST+VLA. The grid spacing was set to 0.5°. Automotive Radar 1 had three transmitters and four receivers, operating at 77 GHz with a bandwidth of 600 MHz. Two corner reflectors are shown in Figure 11. There may be bias in the experimental field measurements. Therefore, we used the maximum likelihood (ML) estimate as the true value, as ML is the optimal estimate under Gaussian noise models [45]. And the ML estimated values are $-4.11°$ and $3.92°$. The number of snapshots was set to 50. By analyzing the radar's calibration matrices, we obtained the equivalent array, with the precise positions of each array element detailed in Table 3.

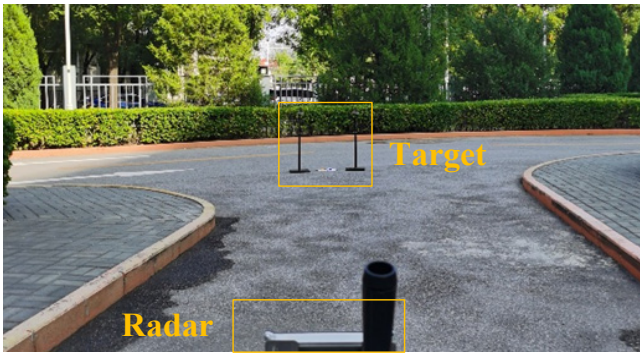


Figure 11. Automotive Radar 1 experimental scenario.

It is evident that the equivalent array is not a standard ULA. Therefore, we could not apply a complete nested array and instead selected some of its elements to form an approximate nested array. We selected $\{1,3,4,5,10,13\}d$ and specify d as the minimum array element spacing, where d is 1.9 mm. The corresponding ideal nested array configuration consists of dense subarray $\{1,2,3,4\}d$ and sparse subarray $\{5,10,15\}d$. Therefore, the positions of the equivalent dense array are denoted as $\{1,3,4\}d$, and those of the equivalent sparse array as $\{5,10,13\}d$. And the actual difference co-array is $\{-12,-10,\cdots,10,12\}d$, which missed the array elements in $\pm 11d$.

The DOA estimation results are presented in Figure 12. As observed, due to the limitations of grid discretization, IST+SLA was unable to reconstruct the two-point targets, whereas the other three algorithms successfully identified both targets. The relative biases were 0.249 for IST+VLA, 0.092 for IVDST+SLA, and 0.025 for IVDST+VLA. Among them, IVDST+VLA had the highest reconstruction accuracy. It is worth noting that if a standardized nested array had been adopted, the reconstruction performance might have been further improved.

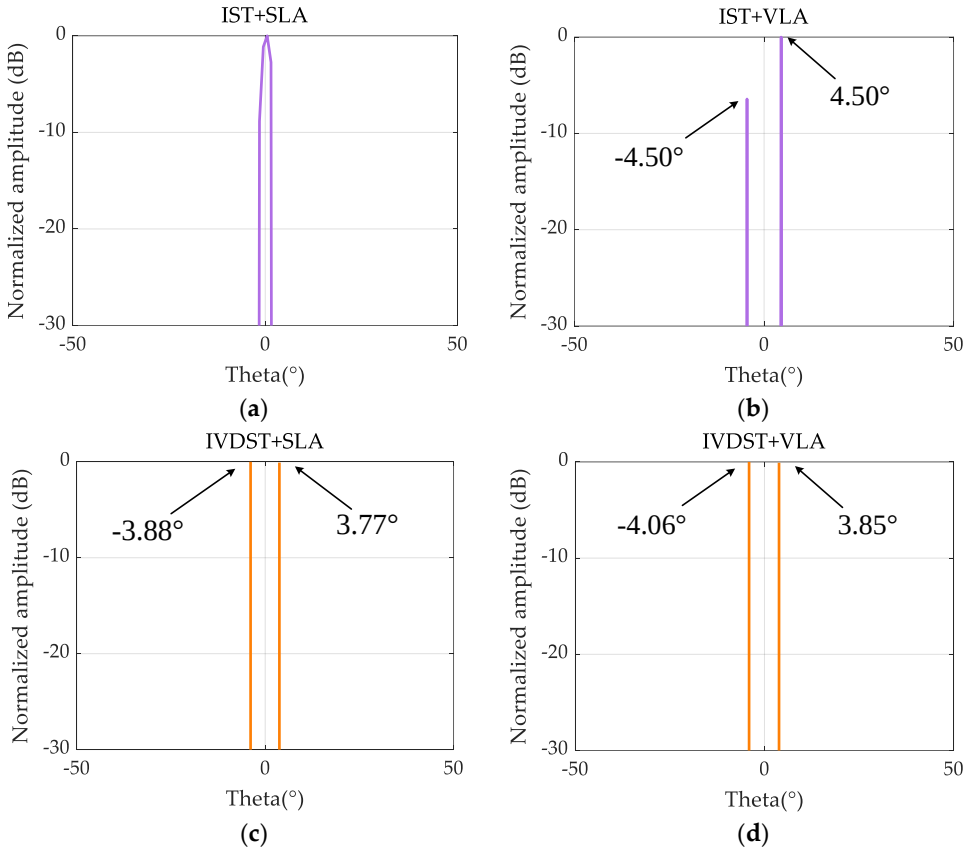


Figure 12. DOA estimation results of IST and IVDST: (**a**) IST+SLA; (**b**) IST+VLA; (**c**) IVDST+SLA; (**d**) IVDST+VLA.

Then, to verify the influence of different sparse array forms on the reconstruction results, we designed three additional sparse arrays, as shown in Table 4. The reconstruction results are shown in Figure 13. Compared with Array 4, the significantly reduced aperture length in Array 1 resulted in unusable estimation results, while the addition of discontinuous virtual elements in Array 2 significantly increased estimation errors. For Array 3, although the number of physical elements was increased, there was no effect on aperture length or the virtual array, thereby maintaining reconstruction accuracy comparable to that of Array 4.

Table 4. The comparison of four different sparse arrays.

	Position	Aperture Length (mm)	Position of Virtual Array	Missing Element	RB
Array 1	$\{1,3,4,5,10\}d$	$9d$	$\{-9,-7,\cdots,7,9\}d$	$\pm 8d$	0.884
Array 2	$\{1,3,4,7,10,13\}d$	$12d$	$\{-12,-10,\cdots,-6,-4,\cdots,4,6,\cdots,10,12\}d$	$\pm 5d, \pm 11d$	0.265
Array 3	$\{1,3,4,5,7,10,13\}d$	$12d$	$\{-12,-10,\cdots,10,12\}d$	$\pm 11d$	0.045
Array 4	$\{1,3,4,5,10,13\}d$	$12d$	$\{-12,-10,\cdots,10,12\}d$	$\pm 11d$	0.025

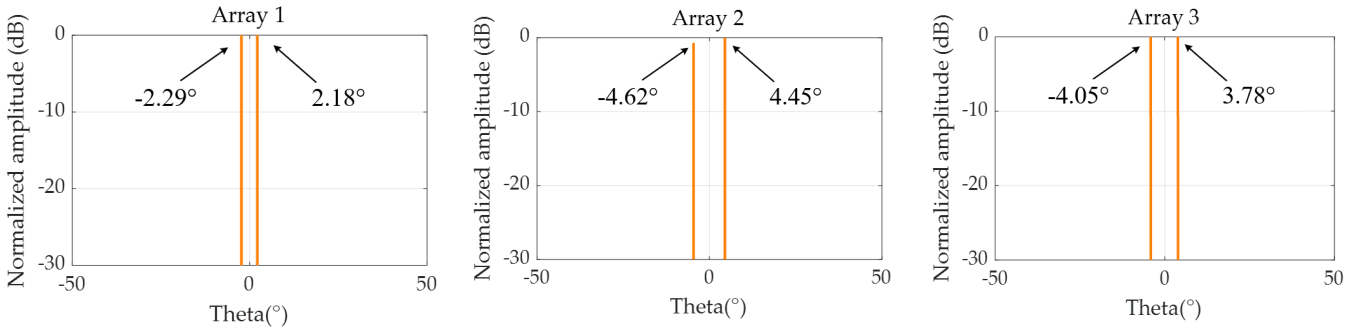


Figure 13. DOA estimation results of different arrays: (**a**) Array 1: $\{1,3,4,5,10\}d$; (**b**) Array 2: $\{1,3,4,7,10,13\}d$; (**c**) Array 3: $\{1,3,4,5,7,10,13\}d$.

Subsequently, we simulated scenarios encountered by Automotive Radar 2 under real road conditions to validate the effectiveness of our proposed algorithm. The experimental setup includes a moving electric vehicle and a stationary motor vehicle on the road. The radar was installed at a height of approximately 80 cm, with the corner reflectors positioned at a similar height. There were streetlights and bushes on either side of the road, and a roadblock was located farther ahead of the vehicle. The radar, designed by Autoroad Tech. Co. Ltd., consists of a MIMO array, including 23 equivalent array elements, as shown in Table 5. Due to the high sparsity of the equivalent array, we selected 17 array elements. The number of snapshots was set to 50.

Table 5. The position of each array in equivalent array and selected array.

	Position (mm)
Equivalent array	$\{0,4,8,12,14,18,30,36,38,40,44,48,52,54,56,62,66,68,78,82,90,102,106\}$
Selected array	$\{0,4,8,12,18,30,36,44,52,56,62,66,78,82,90,102,106\}$

We selected two frames of data obtained during radar operation. As shown in Figure 14, it depicts the actual road during radar sampling. The image was not from the exact sampling moment but was a manually chosen image from a nearby time. The strong scatterers in the experimental scenario mainly include a stationary slanted vehicle A on the right side of the radar, a moving electric bicycle B on the left side, and a streetlight C on the right side. Vehicle A is centrally located at approximately (5.5 m, 27.5 m) with a length of 4.82 m and a width of 1.90 m. The electric bicycle B is located at (−8.6 m, 30.5 m). The streetlight C is located at (8.7 m, 11.4 m).

As shown in Figure 15, our proposed algorithm achieved satisfactory reconstruction results for the first dataset. The center coordinates of vehicle A were approximately (5.12 m, 26.35 m), located in front of and to the right of the radar. The coordinates of electric bicycle B were (−8.41 m, 30.35 m), situated in front of and to the left of the radar. The coordinates of streetlight C were (8.58 m, 11.18 m), located in front of and to the right of the radar. Through analysis of the vehicle in region A, we determined the length of the vehicle to be 4.13 m and its width to be 1.62 m, which aligns with the actual values. In the reconstructed image

Figure 15a, points labeled f1 represent false targets, likely caused by multipath propagation and clutter from other weak targets. The GLRT detector can effectively eliminate these false targets in region f1 while preserving the real targets, as shown in Figure 15b.

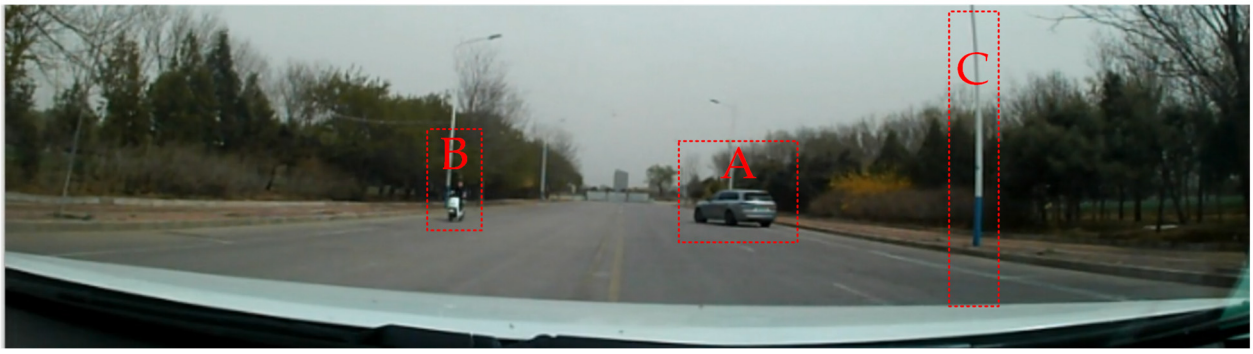
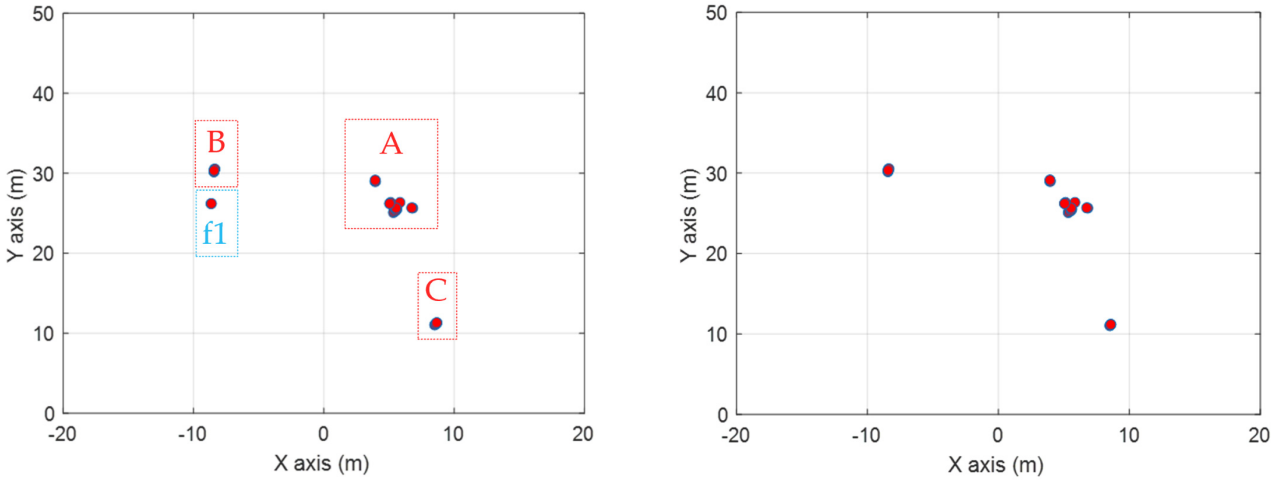


Figure 14. Radar sampling environment for the first dataset. A is the stationary slanted vehicle, B is the moving electric bicycle and C is the streetlight.



(**a**) (**b**)

Figure 15. Reconstructed 2D point cloud image of Figure 14: (**a**) without using GLRT detector; (**b**) using GLRT detector. A is the stationary slanted vehicle, B is the moving electric bicycle, C is the streetlight and f1 is the false target.

As shown in Figure 16, the strong scattering points in the second dataset mainly include two corner reflectors E directly in front the radar, roadblock F at the end of the road, traffic light H and streetlight I on the right side, streetlight G on the left side. The positions of two corner reflectors are (−0.36 m, 5.0 m) and (0.14 m, 5.0 m). Roadblock F was not considered in the experiment, so there are no data available. Streetlight G is located at (−9.0 m, 35.7 m). Traffic light H is located at (8.5 m, 21.2 m). Streetlight I is located at (8.6 m, 12.3 m).

As shown in Figure 17, the coordinates of two corner reflectors were (−0.37 m, 4.93 m) and (0.14 m, 4.94 m), located 4.94 m directly in front of the radar. The roadblock F was positioned 40.69 m ahead of the radar, with a lateral length of approximately 6.62 m. Streetlight G was located at (−8.79 m, 35.52 m) in the front-left direction of the radar. Traffic light H was positioned at (8.17 m, 21.61 m) in the front-right direction of the radar. Streetlight I was located at (8.60 m, 12.29 m) to the front-right of the radar.

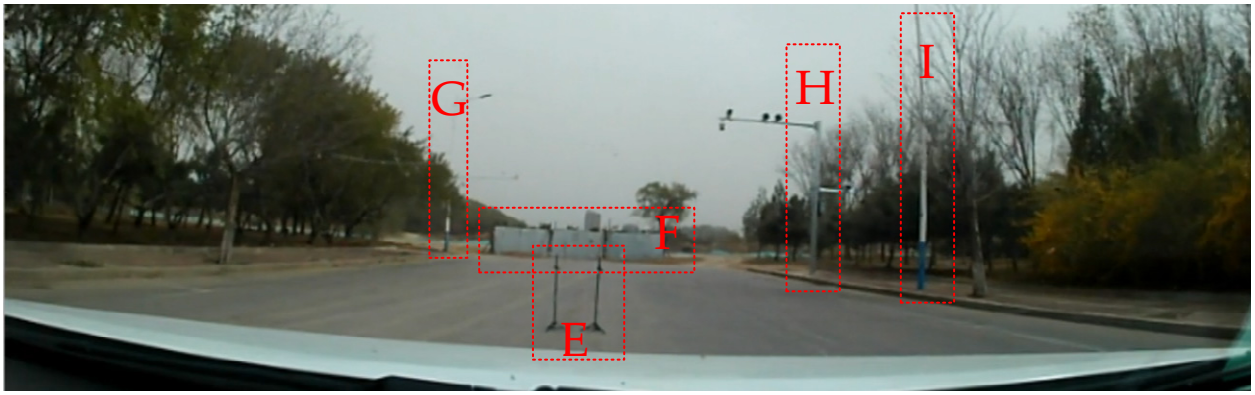
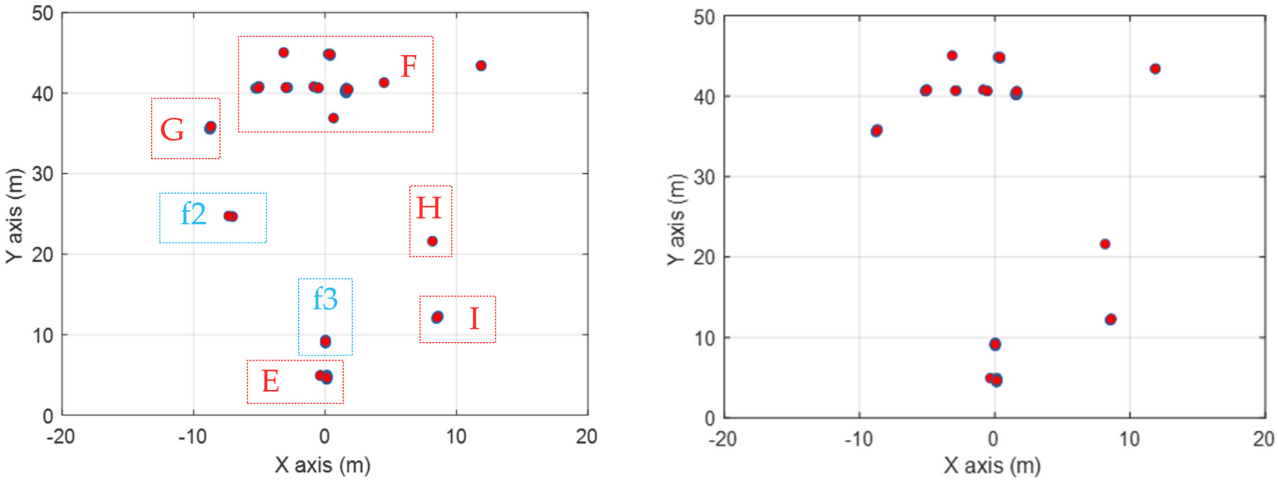


Figure 16. Radar sampling environment for the second dataset. E is the two corner reflectors, F is the roadblock, G is the streetlight, H is the traffic light, and I is the streetlight.



(**a**) (**b**)

Figure 17. Reconstructed 2D point cloud image of Figure 16: (**a**) without using GLRT detector; (**b**) using GLRT detector. E is the two corner reflectors, F is the roadblock, G is the streetlight, H is the traffic light, I is the streetlight, and f2, f3 are the false targets.

Our proposed algorithm achieved satisfactory reconstruction results. The distance between the two corner reflectors was measured to be 0.51 m, which is consistent with the actual value. The GLRT detector effectively eliminates false targets in the f2 region. However, false targets in the f3 region remained. We analyzed the raw sampling data and found that the false targets in the f3 area had strong echo intensity and a relative motion speed of 7 km/h relative to the vehicle. We believe this was caused by unforeseeable factors in the experimental environment, therefore, the GLRT detector could not eliminate these false targets.

6. Discussion

In this work, both simulation experiments and real data experiments have validated the effectiveness of the algorithm proposed in this paper. We conducted three sets of simulation experiments to comparatively analyze the algorithm's gridless reconstruction performance, noise resistance, and super-resolution capabilities. These results consistently demonstrate the proposed algorithm's superiority over the existing methods. Additionally, we analyzed the impact of the number of snapshots and the number of point targets on the algorithm's reconstruction performance. These two parameters play a crucial role in ensuring that the algorithm operates within its optimal performance range. Subsequently,

we examined the algorithm's computational efficiency to ensure it meets the real-time requirements of automotive radar applications. Compared with the traditional ANM algorithm, our proposed algorithm reduces the computational complexity by approximately 1.5 orders of magnitude. Finally, we designed two sets of real data experiments. The reconstruction results shown in Figure 12 validate the excellent reconstruction performance of the algorithm in real-world environments, significantly improving reconstruction accuracy compared to grid-based algorithms. Figures 15 and 17 demonstrate the proposed algorithm's reconstruction capability in real road environments, achieving high-precision road target reconstruction. Moreover, the introduction of the GLRT detector eliminates the impact of weak targets and clutter, enhancing the usability of the reconstructed images.

In summary, our proposed algorithm can reduce the cost and operating time of automotive radars while ensuring reconstruction performance, demonstrating strong practical value. Although the proposed algorithm successfully achieves the expected goals, there are still opportunities for further optimization. Firstly, we can validate the algorithms on a wider range of real-world road scenarios, such as more complex urban roads. Then, the automotive radar model used in this paper has not undergone nested array design; thus, it cannot achieve the algorithm's optimal performance. Finally, as the goal of this paper is to explore the potential application of our proposed algorithm in automotive radar, the impact of multipath propagation on the reconstruction results has not been discussed. Therefore, further validation is needed using automotive radars that meet the requirements of nested array designs.

7. Conclusions

Millimeter-wave automotive radars possess the capability to obtain road surface information around the clock and under all weather conditions. Concurrently, the continuous advancements in autonomous driving technology have imposed higher performance requirements on radars. To address the challenges of reducing costs and improving reconstruction performance in automotive radar, this paper proposed a sparse reconstruction algorithm for automotive radar based on accelerated ANM. We applied sparse array to automotive radar, utilizing difference co-array to obtain virtual elements with more array elements and a longer aperture, thereby reducing costs while ensuring subsequent sparse reconstruction performance. To further enhance the reconstruction performance, we introduced the IVDST algorithm, which effectively mitigates the problems of off-grid targets and high computational complexity. Finally, we used the GLRT detector to process the noise and clutter in the operating environment of automotive radar, effectively eliminating the influence of clutter and weak targets on the imaging results.

We conducted a detailed comparison of the performance between the proposed algorithm and other algorithms through simulation experiments. The results from both single simulation experiments and Monte Carlo simulation experiments confirmed the superiority of the proposed algorithm. Furthermore, we validated the effectiveness of the algorithm in practical applications through two sets of real-world data experiments. In future work, we will conduct detailed experiments to evaluate the practical reconstruction performance of automotive radar in complex scenarios. Additionally, we will explore more advanced sparse array configurations, such as Augmented Nested Array [46] and MISC Array [47]. We wish to further reduce costs while maintaining superior reconstruction performance.

Author Contributions: Conceptualization, P.J. and Z.Z.; methodology, P.J., S.G. and Z.Z.; software, P.J. and S.G.; validation, P.J., S.G., J.Z. and Z.Z.; formal analysis, P.J.; investigation, P.J. and Z.Z.; resources, Z.Z. and B.Z.; data curation, J.Z. and Z.Z.; writing—original draft preparation, P.J., S.G. and Z.Z.; writing—review and editing, P.J., S.G., Z.Z. and B.Z.; visualization, P.J; supervision, P.J. and Z.Z.; project administration, Z.Z. All authors have read and agreed to the published version of the manuscript.

Funding: This research received no external funding.

Data Availability Statement: The original contributions presented in the study are included in the article, further inquiries can be directed to the corresponding author.

Conflicts of Interest: Author Jie Zhao was employed by the company Beijing Autoroad Tech Company, Ltd. The remaining authors declare that the research was conducted in the absence of any commercial or financial relationships that could be construed as a potential conflict of interest.

References

1. Patole, S.M.; Torlak, M.; Wang, D.; Ali, M. Automotive radars: A review of signal processing techniques. *IEEE Signal Process. Mag.* **2017**, *34*, 22–35. [CrossRef]
2. Engels, F.; Heidenreich, P.; Wintermantel, M.; Stäcker, L.; Kadi, M.A.; Zoubir, A.M. Automotive Radar Signal Processing: Research Directions and Practical Challenges. *IEEE J. Sel. Top. Signal Process.* **2021**, *15*, 865–878. [CrossRef]
3. Stateczny, A.; Kazimierski, W.; Gronska-Sledz, D.; Motyl, W. The Empirical Application of Automotive 3D Radar Sensor for Target Detection for an Autonomous Surface Vehicle's Navigation. *Remote Sens.* **2019**, *11*, 1156. [CrossRef]
4. Waldschmidt, C.; Hasch, J.; Menzel, W. Automotive Radar—From First Efforts to Future Systems. *IEEE J. Microw.* **2021**, *1*, 135–148. [CrossRef]
5. Hasch, J.; Topak, E.; Schnabel, R.; Zwick, T.; Weigel, R.; Waldschmidt, C. Millimeter-Wave Technology for Automotive Radar Sensors in the 77 GHz Frequency Band. *IEEE Trans. Microw. Theory Tech.* **2012**, *60*, 845–860. [CrossRef]
6. Tan, B.; Ma, Z.; Zhu, X.; Li, S.; Zheng, L.; Huang, L.; Bai, J. Tracking of Multiple Static and Dynamic Targets for 4D Automotive Millimeter-Wave Radar Point Cloud in Urban Environments. *Remote Sens.* **2023**, *15*, 2923. [CrossRef]
7. Yang, H.; She, M.; Li, T.; Yan, W.; Cheng, Y.; Li, N.; Pu, S.; Shen, L.; Shen, L.; Qian, T. A Genetic-Algorithm-Based Sparse Planar Array Optimization Method for 77 GHz High-Resolution Imaging. In Proceedings of the 2022 IEEE International Symposium on Antennas and Propagation and USNC-URSI Radio Science Meeting (AP-S/URSI), Denver, CO, USA, 10–15 July 2022; pp. 145–146. [CrossRef]
8. Correas-Serrano, A.; González-Huici, M.A. Experimental Evaluation of Compressive Sensing for DoA Estimation in Automotive Radar. In Proceedings of the 2018 19th International Radar Symposium (IRS), Bonn, Germany, 20–22 June 2018; pp. 1–10. [CrossRef]
9. Zhang, W.; He, N.; He, Z.; Han, M. Approach of 2D direction of arrival estimation of FMCW traffic radar by utilising 1D array. *Electron. Lett.* **2020**, *56*, 97–99. [CrossRef]
10. Wang, X.; Zhai, W.; Zhang, X.; Wang, X.; Amin, M.G. Enhanced Automotive Sensing Assisted by Joint Communication and Cognitive Sparse MIMO Radar. *IEEE Trans. Aerosp. Electron. Syst.* **2023**, *59*, 4782–4799. [CrossRef]
11. Sun, S.; Zhang, Y.D. 4D Automotive Radar Sensing for Autonomous Vehicles: A Sparsity-Oriented Approach. *IEEE J. Sel. Top. Signal Process.* **2021**, *15*, 879–891. [CrossRef]
12. Sun, S.; Zhang, Y.D. Four-Dimensional High-Resolution Automotive Radar Imaging Exploiting Joint Sparse-Frequency and Sparse-Array Design. In Proceedings of the ICASSP 2021—2021 IEEE International Conference on Acoustics, Speech and Signal Processing (ICASSP), Toronto, ON, Canada, 6–11 June 2021; pp. 8413–8417. [CrossRef]
13. Moffet, A. Minimum-redundancy linear arrays. *IEEE Trans. Antennas Propag.* **1968**, *16*, 172–175. [CrossRef]
14. Vaidyanathan, P.P.; Pal, P. Theory of Sparse Coprime Sensing in Multiple Dimensions. *IEEE Trans. Signal Process.* **2011**, *59*, 3592–3608. [CrossRef]
15. Pal, P.; Vaidyanathan, P.P. Nested Arrays: A Novel Approach to Array Processing With Enhanced Degrees of Freedom. *IEEE Trans. Signal Process.* **2010**, *58*, 4167–4181. [CrossRef]
16. Pal, P.; Vaidyanathan, P.P. Coprime sampling and the music algorithm. In Proceedings of the 2011 Digital Signal Processing and Signal Processing Education Meeting (DSP/SPE), Sedona, AZ, USA, 4–7 January. 2011; pp. 289–294. [CrossRef]
17. Lutz, S.; Ellenrieder, D.; Walter, T.; Weigel, R. On fast chirp modulations and compressed sensing for automotive radar applications. In Proceedings of the 2014 15th International Radar Symposium (IRS), Gdansk, Poland, 16–18 June 2014; pp. 1–6. [CrossRef]
18. Lee, S.; Jung, Y.; Lee, M.; Lee, W. Compressive Sensing-Based SAR Image Reconstruction from Sparse Radar Sensor Data Acquisition in Automotive FMCW Radar System. *Sensors* **2021**, *21*, 7283. [CrossRef] [PubMed]
19. Jung, D.H.; Kang, H.S.; Kim, C.K.; Park, J.; Park, S.O. Sparse Scene Recovery for High-Resolution Automobile FMCW SAR via Scaled Compressed Sensing. *IEEE Trans. Geosci. Remote Sens.* **2019**, *57*, 10136–10146. [CrossRef]
20. Roldan, I.; Lamberti, L.; Fioranelli, F.; Yarovoy, A. Low Complexity Single-Snapshot DoA Estimation via Bayesian Compressive Sensing. In Proceedings of the 2023 IEEE Radar Conference (RadarConf23), San Antonio, TX, USA, 1–5 May 2023; pp. 1–6. [CrossRef]
21. Chi, Y.; Scharf, L.L.; Pezeshki, A.; Calderbank, A.R. Sensitivity to Basis Mismatch in Compressed Sensing. *IEEE Trans. Signal Process.* **2011**, *59*, 2182–2195. [CrossRef]
22. Wu, X.; Zhu, W.-P.; Yan, J.; Zhang, Z. Two sparse-based methods for off-grid direction-of-arrival estimation. *Signal Process.* **2018**, *142*, 87–95. [CrossRef]

23. Wagner, M.; Park, Y.; Gerstoft, P. Gridless DOA Estimation and Root-MUSIC for Non-Uniform Linear Arrays. *IEEE Trans. Signal Process.* **2021**, *69*, 2144–2157. [CrossRef]
24. Jiang, H.; Tang, W.-G.; Pang, S.-X. Off-grid DOA estimation for nested array using atomic norm minimisation. *Electron. Lett.* **2018**, *54*, 1344–1346. [CrossRef]
25. Tang, G.; Bhaskar, B.N.; Shah, P.; Recht, B. Compressed Sensing Off the Grid. *IEEE Trans. Inf. Theory* **2013**, *59*, 7465–7490. [CrossRef]
26. Chen, T.; Shi, L.; Guo, L. Gridless Direction of Arrival Estimation Exploiting Sparse Linear Array. *IEEE Signal Process. Lett.* **2020**, *27*, 1625–1629. [CrossRef]
27. Wu, X.; Zhu, W.P. Single Far-Field or Near-Field Source Localization With Sparse or Uniform Cross Array. *IEEE Trans. Veh. Technol.* **2020**, *69*, 9135–9139. [CrossRef]
28. Wang, F.; Tian, Z.; Leus, G.; Fang, J. Direction of Arrival Estimation of Wideband Sources Using Sparse Linear Arrays. *IEEE Trans. Signal Process.* **2021**, *69*, 4444–4457. [CrossRef]
29. Gao, S.; Wang, M.; Zhang, Z.; Zhang, B.; Wu, Y. Efficient Gridless DOA Estimation for Nonuniformly Spaced Linear Arrays in Automotive Radar Sensors. *IEEE Sens. J.* **2024**, *24*, 27737–27749. [CrossRef]
30. Yang, Z.; Xie, L. On Gridless Sparse Methods for Line Spectral Estimation From Complete and Incomplete Data. *IEEE Trans. Signal Process.* **2015**, *63*, 3139–3153. [CrossRef]
31. Wang, Y.; Tian, Z. IVDST: A Fast Algorithm for Atomic Norm Minimization in Line Spectral Estimation. *IEEE Signal Process. Lett.* **2018**, *25*, 1715–1719. [CrossRef]
32. Liu, N.; Li, X.; Peng, X.; Hong, W. SAR Tomography Based on Atomic Norm Minimization in Urban Areas. *Remote Sens.* **2022**, *14*, 3439. [CrossRef]
33. Zheng, L.; Long, J.; Lops, M.; Liu, F.; Hu, X.; Zhao, C. Detection of Ghost Targets for Automotive Radar in the Presence of Multipath. *IEEE Trans. Signal Process.* **2024**, *72*, 2204–2220. [CrossRef]
34. Kelly, E.J. An Adaptive Detection Algorithm. *IEEE Trans. Aerosp. Electron. Syst.* **1986**, *AES-22*, 115–127. [CrossRef]
35. Robey, F.C.; Fuhrmann, D.R.; Kelly, E.J.; Nitzberg, R. A CFAR adaptive matched filter detector. *IEEE Trans. Aerosp. Electron. Syst.* **1992**, *28*, 208–216. [CrossRef]
36. Budillon, A.; Johnsy, A.C.; Schirinzi, G. Extension of a Fast GLRT Algorithm to 5D SAR Tomography of Urban Areas. *Remote Sens.* **2017**, *9*, 844. [CrossRef]
37. Liu, W.; Budillon, A.; Pascazio, V.; Schirinzi, G.; Xing, M. Performance Improvement for SAR Tomography Based on Local Plane Model. *IEEE J. Sel. Top. Appl. Earth Obs. Remote Sens.* **2022**, *15*, 2298–2310. [CrossRef]
38. Fortunati, S.; Grasso, R.; Gini, F.; Greco, M.S.; LePage, K. Single-snapshot DOA estimation by using Compressed Sensing. *EURASIP J. Adv. Signal Process.* **2014**, *2014*, 120. [CrossRef]
39. Pal, P.; Vaidyanathan, P.P. Nested Arrays in Two Dimensions, Part II: Application in Two Dimensional Array Processing. *IEEE Trans. Signal Process.* **2012**, *60*, 4706–4718. [CrossRef]
40. Williams, R.T.; Prasad, S.; Mahalanabis, A.K.; Sibul, L.H. An improved spatial smoothing technique for bearing estimation in a multipath environment. *IEEE Trans. Acoust. Speech Signal Process.* **1988**, *36*, 425–432. [CrossRef]
41. Bhaskar, B.N.; Tang, G.; Recht, B. Atomic Norm Denoising With Applications to Line Spectral Estimation. *IEEE Trans. Signal Process.* **2013**, *61*, 5987–5999. [CrossRef]
42. Zhang, Z.; Wang, Y.; Tian, Z. Efficient two-dimensional line spectrum estimation based on decoupled atomic norm minimization. *Signal Process.* **2019**, *163*, 95–106. [CrossRef]
43. Gao, S.; Zhang, Z.; Zhang, B.; Wu, Y. Gridless tomographic SAR imaging based on accelerated atomic norm minimization with efficiency. In Proceedings of the International Conference on Radar Systems (RADAR 2022), Edinburgh, UK, 24–27 October 2022; pp. 48–53. [CrossRef]
44. Lee, J.; Li, Y.A.; Hung, M.H.; Huang, S.J. A Fully-Integrated 77-GHz FMCW Radar Transceiver in 65-nm CMOS Technology. *IEEE J. Solid-State Circuits* **2010**, *45*, 2746–2756. [CrossRef]
45. Stoica, P.; Sharman, K.C. Maximum likelihood methods for direction-of-arrival estimation. *IEEE Trans. Acoust. Speech Signal Process.* **1990**, *38*, 1132–1143. [CrossRef]
46. Liu, J.; Zhang, Y.; Lu, Y.; Ren, S.; Cao, S. Augmented Nested Arrays With Enhanced DOF and Reduced Mutual Coupling. *IEEE Trans. Signal Process.* **2017**, *65*, 5549–5563. [CrossRef]
47. Zheng, Z.; Wang, W.-Q.; Kong, Y.; Zhang, Y.D. MISC Array: A New Sparse Array Design Achieving Increased Degrees of Freedom and Reduced Mutual Coupling Effect. *IEEE Trans. Signal Process.* **2019**, *67*, 1728–1741. [CrossRef]

Disclaimer/Publisher's Note: The statements, opinions and data contained in all publications are solely those of the individual author(s) and contributor(s) and not of MDPI and/or the editor(s). MDPI and/or the editor(s) disclaim responsibility for any injury to people or property resulting from any ideas, methods, instructions or products referred to in the content.